Journal of the European Ceramic Society 44 (2024) 5579–5589

Contents lists available at ScienceDirect

Journal of the European Ceramic Society

journal homepage: www.elsevier.com/locate/jeurceramsoc

A bi-phasic numerical approach for non-linear response and stiffness recovery related to residual thermal stress in UHTCMCs

Antonio Maria Caporale [a], Pietro Galizia [b,*], Bartolomeo Zanardi [a,b], Antonio Vinci [b], Diletta Sciti [b], Alessandro Airoldi [a]

[a] Department of Aerospace Science and Technology, Politecnico di Milano, Via La Masa, 34, Milano 20156, Italy
[b] National Research Council of Italy - Institute of Science, Technology and Sustainability for Ceramics (CNR - ISSMC; former ISTEC), Via Granarolo 64, Faenza 48018, Italy

ARTICLE INFO

Keywords:
Ceramic matrix composites (CMCs)
Mechanical properties
Residual stresses
Plasticity
Drucker-Prager, UHTCMC

ABSTRACT

The tensile properties of sintered C_f-ZrB_2/SiC UHTCMCs were investigated for different lamination sequences, revealing ultimate strengths of 570 MPa (0°/0°), 120 MPa (0°/90°), and 40 MPa (90°/90°). The results facilitated modeling the material's non-linear tensile response, characterized by a remarkably prolonged plateau with pseudo-plastic behavior, followed by stiffness recovery before ultimate failure. A simplified analytical model was developed to predict this behavior originated by residual thermal stresses and inelastic phenomena. A complete constitutive law was then developed and implemented in a FE model, utilizing a bi-phasic approach including Drucker-Prager plasticity and orthotropic ductile damage. Two-step analyses were performed, starting with a thermal step to represent the buildup of a self-equilibrating RTS state in the material phases, followed by a mechanical simulation. This demonstrated the model's efficacy in capturing the non-linear response in both homogeneous and cross-ply lay-ups, contributing to advancements in materials engineering and the design of UHTCMCs-based hot structures.

1. Introduction

Atmospheric reentry is one of the critical phases in the operative life of reusable space vehicles, due to the harsh condition which combines ultra-high temperature with oxidative environment at low oxygen partial pressure [1–4]. Ultra High Temperature CMCs (UHTCMCs) are special composites with a dense matrix made of ultra refractory ceramics, the so called UHTCs (broadly borides and carbides of early transition metals). A number of studies has been published in the last five years on sintered UHTCMCs, concerning microstructure, mechanical and ablation behavior [5–20] and among them, ZrB_2-based UHTCMCs have shown the best tradeoff between oxidation/ablation resistance and density. In a previous work, it was outlined that the substantial coefficient of thermal expansion (CTE) mismatch, robust bonding at the fiber/matrix interface, and the pressure-assisted sintering process collectively resulted in a residual compressive strain along the longitudinal direction of the fibers. This compressive strain was effectively counterbalanced by the UHTC-matrix, maintaining an average residual tensile stress close to the theoretical critical value [21].

Moreover. considering the analysis of tangent stiffness evolution in bending tests it was also hypothesized that the tensile stresses within the UHTC matrix, close to the strength of corresponding monolithic ceramic, led to premature damage in the matrix allowing the release of the compressive stresses in fiber [21]. Such phenomenon could be considered the driving mechanism for the ductile response of the material, which was evidenced both in bending and tensile tests performed on laminates with a homogeneous $[0]_n$ lay-ups: the stress vs. strain curve presents a knee with a remarkable reduction of the tangent modulus followed by a final recovery of the stiffness before the final failure [21,22].

Such type of response led to a peculiar S-shape response, which had been observed and related to RTSs in other CMCs, such as in [23,24], but with much lower variation in the tangent moduli of the materials. Moreover, the experimental results in [21,22] clearly indicate that this behavior tend to disappear in tests performed at high temperature, thus confirming the role of the RTSs in phenomenon.

The relevancy of these non-linear effects in the material response motivate the development of analytical and numerical approach for

* Corresponding author.
E-mail address: pietro.galizia@cnr.it (P. Galizia).

https://doi.org/10.1016/j.jeurceramsoc.2024.03.038
Received 16 February 2024; Accepted 12 March 2024
Available online 15 March 2024

quantitative predictions, which are deemed particularly important for the design of UHTCMCs elements with structural role considering a damage tolerant approach, that is taking into account the possibility that part of the structure could exceed the limit of linear response, due to reasons such as manufacturing defects, damages, or low-energy impacts.

Actually, numerical approaches were implemented to model the presence of RTS in $C_f - ZrB_2/SiC$ UHTCMC, with a Reference Volume Element (RVE) method [25] or at the mesoscale [20,26]. Moreover, a RVE method was used to study the toughening mechanisms of pyrolytic carbon interface layer [27]. However, these models were not aimed at interpreting and modelling the role of RTSs and of matrix and fiber-matrix interface damage on the peculiar non-linear response of UHTCMCs for engineering applications.

The present work was focused on a more systematic characterization of the tensile response of UHTCMCs laminates, considering loading-unloading cycles on $[0]_8$, $[0/90]_{3S}$, and $[90]_8$ lay-ups to obtain the data necessary for the development of a macroscale non-linear model of the material. Specimens were sintered in one of the largest machines available in Europe that allows to produce disks of 400 mm diameter [12]. In this way all the mechanically tested specimens were extracted from the same sintered piece despite their large dimensions.

For the development of the model, the study of the non-linear phenomena and the qualitative interpretations given in [21,22,28,29] pointed towards the need of representing the self-equilibrating RTS state built in the material during the manufacturing and the adoption of non-linear response for the matrix phase.

Such approach required the decomposition of the material into two simplified constitutive phases with different CTEs, in a way similar to the Binary models developed by Cox et al., [30,31], which was successfully assessed for a C/SiC [32] and SiC/SiC CMC [33]. The peculiarity of the Binary Model is the decomposition of the material in two idealized constituents to separately model the properties of a reinforcement phase and an effective medium phase. In a similar way, Airoldi et al. developed a bi-phasic modeling technique that allows the modelling of both in-plane and out-of-plane nonlinearities in polymeric and graphitic matrix composites [34].

Before developing the model, a quantitative analytical interpretation of the response was formalized by using a simple analytical micromechanical approach based on the rule of mixture. Thereafter, a complete bi-phasic model of the material, including an elastic-plastic damageable matrix phase, was developed and implemented in constitutive law to be used in the commercial Abaqus/Explicit finite element solver code, simulating both the build-up of RTSs in the two idealized phases and the subsequent mechanical response for unidirectional and cross-ply laminates.

This article is organized in six sections. After this introduction, the material and the specimens are presented and discussed, including a microstructural analysis of the $C_f - ZrB_2/SiC$ UHTCMCs. Then, the results of the experimental tensile characterization at room temperature are reported, with particular attention to the nonlinear behaviors and the residual deformations in a third section. In the fourth section, an analytical interpretation of the material nonlinearities and residual strain based on RTS is presented. In the fifth section, a finite element bi-phasic approach is implemented in Abaqus/Explicit code, which from one hand has to be predictive of the nonlinear stress trends of the material and on the other hand has to represent, clarify, and extend the analytical interpretation here presented. The findings of the activity are finally summarized in the sixth section.

2. Materials and specimens

2.1. Specimen production

Cf- ZrB_2 -SiC UHTCMCs were produced by slurry impregnation and sintering according to previous works [12,13,35,36]. Discs with a diameter of 400 mm underwent consolidation through spark plasma sintering, followed by precision machining to produce a comprehensive array of bars with varying lengths and shapes, extending up to 200 mm. These bars were prepared for subsequent tensile characterization, as detailed in Table 1.

2.2. Tensile test campaign

Tensile tests at room temperature were performed on three different family of specimens with lamination sequences $[0]_{12}$, $[0/90]_{12}$, $[90]_{12}$, called T0, T090 and T90, respectively. ASTM C1275–15 was used as reference. The aim was to investigate the in-plane elastic response, the nonlinear behaviors, and the failure properties of UHTCMC. The numbers, lamination sequences and dimensions of the specimens are reported in Table 1. T0 and T90 specimens were dog-bone shaped, while T090 was not. In the T090 specimen, it was decided to analyze the progressive damage accumulation in the whole volume of the specimen, trying to avoid the specific state of stress in the zone of section variation could lead to a localization of damage. Four $4mm$ thick tapered tabs laminated by using glass/epoxy plies with lamination sequence $[45]_{13}$ where sticked to the specimens, two at each extremity, using a hot-curing Scotch Weld AFK 163–2 K structural adhesive epoxy tape. The tapering was produced by machining a laminate with an angle of $14 \pm 1°$ as prescribed by the standard. Tabs were needed to distribute the stress introduced by the testing machine clamps into the specimen, avoiding unwanted stress concentrations. An example of each family of specimens is reported in Fig. 1.

An MTS 810 Material Testing System was used together with an extensometer placed on the specimen and an acquisition system that sampled the applied force, the crosshead displacement, and the extensometer signal. A sampling frequency of $10kHz$ was set and a fixed crosshead displacement velocity of $0.5mm/\mathrm{min}$ was imposed. Several loading/unloading cycles were performed in each test to evaluate the presence of residual deformations.

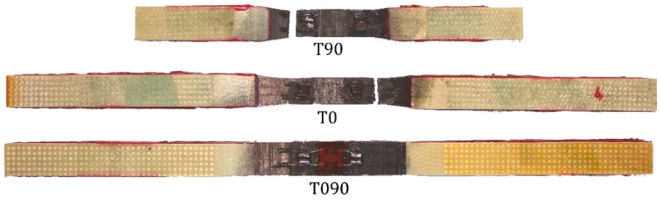

Fig. 1. Example of UHTCMC tensile specimens, one per each family, T90, T0, and T090, with fiberglass tabs to avoid excessive stress concentration.

Table 1
Specimen ID and corresponding fiber architecture, geometry and tensile configuration.

Specimen	Number	Lamination sequence	Dogbone shape	Length (mm)	Gage length (mm)	Thickness (mm)	Width (mm)	Gage width (mm)
T0	5	$[0]_8$	Yes	200	144	2.47 ± 0.01	10.00 ± 0.03	7.97 ± 0.03
T090	4	$[0/90]_{3s}$	No	200	–	3.98 ± 0.04	10.00 ± 0.06	–
T90	5	$[90]_8$	Yes	100	36	2.48 ± 0.01	10.01 ± 0.03	8.02 ± 0.05

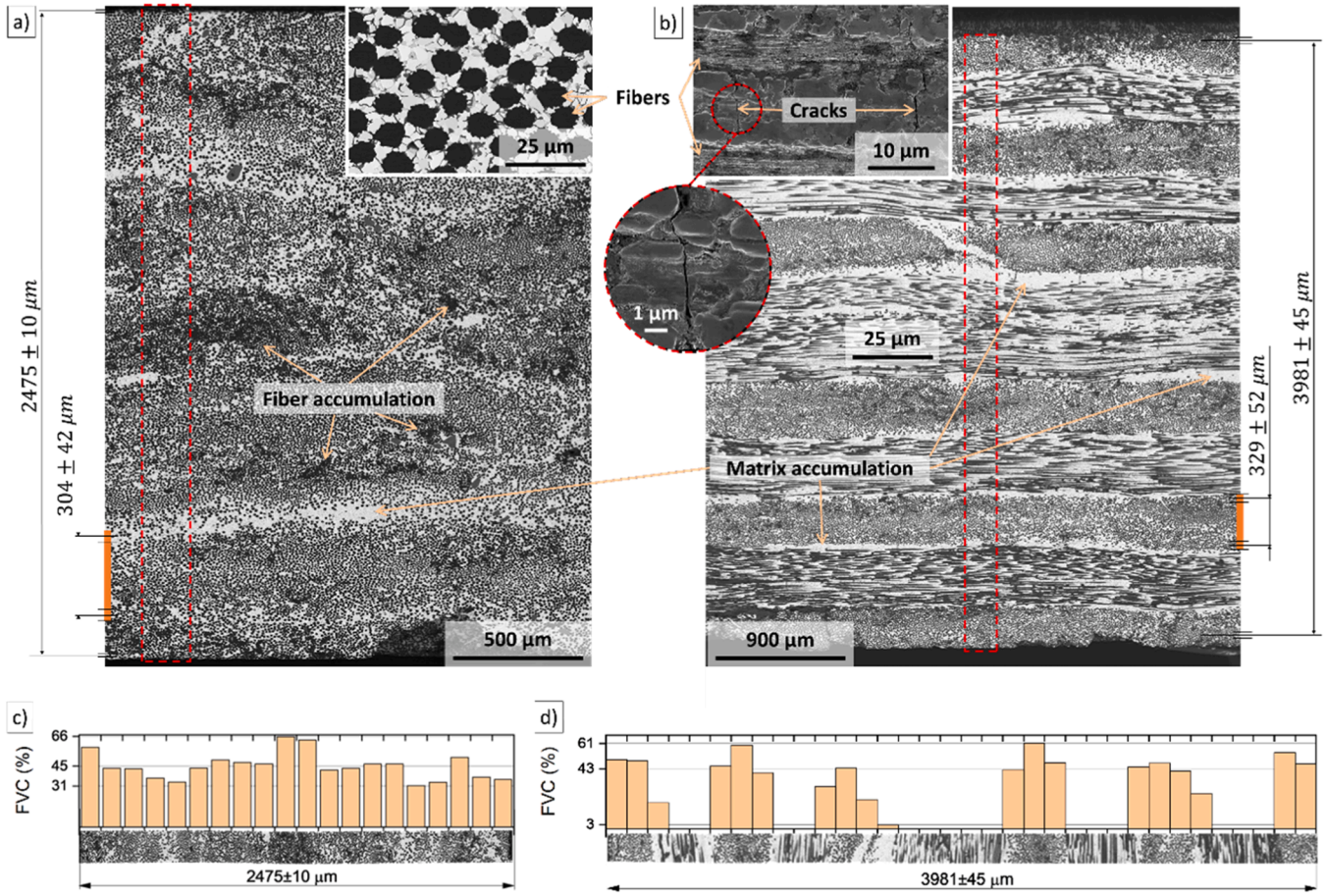

Fig. 2. SEM images of polished cross-section of a (a) T0 and (b) T090 specimen. The light grey areas and the dark grey areas correspond to the matrix and the pitch-derived carbon fibers. The insets show zooms along the (a) longitudinal direction and (b) transverse direction of a single unidirectional layer. The average thickness of a single layer, together with the average thickness of the tensile specimens, is reported beside the low magnification micrographs. The area highlighted with dashed line was mapped with micrographs at 2000x and used to measure the volumetric fiber content (FVC). Each measured FVC-value is reported as a bar in the graphs (c) and (d) above to the investigated area. In the y-axis the max, weighted mean and min FVC-value is reported.

2.3. Microstructural features of the coupons

The microstructure of sintered UHTCMCs was analyzed on polished and fractured surfaces by field emission scanning electron microscopy (FE-SEM, Carl Zeiss Sigma NTS GmbH Öberkochen, Germany). Volumetric fiber amount was measured by image analysis (Image-Pro Analyzer 7.0, v.7, Media Cybernetics, USA) of polished sections. In particular, an area of about $200 \times 2500 \mu m^2$ at 2000x magnification was mapped for 0°/0° material and an area of $200 \times 4000 \mu m^2$ for 0°/90° material to cover the entirely thickness of the specimens. In case of 0°/90°, V_f was measured only on the micrographs with out-of-plane fibers.

The average thickness of the single layer was calculated excluding the machined outermost layers of all the specimens produced for the mechanical tests.

Typical microstructures of sintered 0°/0° and 0°/90° materials are illustrated in Fig. 2. Both composites showed the absence of macro-porous and the typical strong fiber/matrix interface characterized by the jagged borders [37]. The main difference between the two composites consisted in the fiber/matrix distribution. On one hand, 0°/0° composite showed a lower fiber dispersion as evidenced in Fig. 2a by the dark spots that are groups of fibers. On the other hand, 0°/90° composite showed thicker layers of unreinforced matrix regions that appear between the infiltrated preforms (see Fig. 2b). These differences led to a higher fiber amount in the 0°/0° composite (45% *vs* 43%, in Fig. 2c and d it can be seen also the variation of fiber amount through the entire thickness) and higher layer thickness in the 0°/90° composite (about 300 µm *vs* 330 µm). This difference in thickness could be explained with the settling down of the fibers in 0°/0° composite when the pressure is applied during the manufacturing process. In the case of 0°/90° composite, the presence of transverse fibers limits the displacement of the longitudinal ones. It is widely acknowledged that the mismatch in CTE between the ceramic matrix and fiber results in micro-cracking within

Table 2
Density (ρ), porosity (P), fiber volumetric content (V_f) with longitudinal (0°) and transversal (90°) orientation, layer thickness (t), dynamic Young's (E) and shear modulus (G) of the two ∅400*mm* disks produced with lamination sequences oriented at 0° and 0°/90°.

Material	ρ	P	V_f		T	E	G
			0°	90°			
	(g/cm^3)	(%)	(%)	(%)	(µm)	(GPa)	(GPa)
0°/0°	3.83 ± 0.05	9	45	0	304 ± 42	324 ± 4	47 ± 1
0°/90°	3.67 ± 0.10	13	20	23	329 ± 52	130 ± 8	37 ± 4

Table 3
Results of the tensile tests: elastic modulus of three stages (E_I, E_{II} and E_{III}); yield strength (σ_y); ultimate strength (σ_U); yield strain (ε_y); ultimate strain (ε_U).

Specimen	E_I (GPa)	E_{II} (GPa)	E_{III} (GPa)	σ_y (MPa)	σ_U (MPa)	ε_y (με)	ε_U (με)
T0	272 ± 4	63 ± 5	256 ± 11	36 ± 6	568 ± 28	122 ± 28	3419 ± 78
T090	131 ± 17	8 ± 1	99 ± 49	17 ± 3	121 ± 36	150 ± 23	5905 ± 407
T90	74 ± 3	-	-	-	40 ± 12	-	597 ± 207

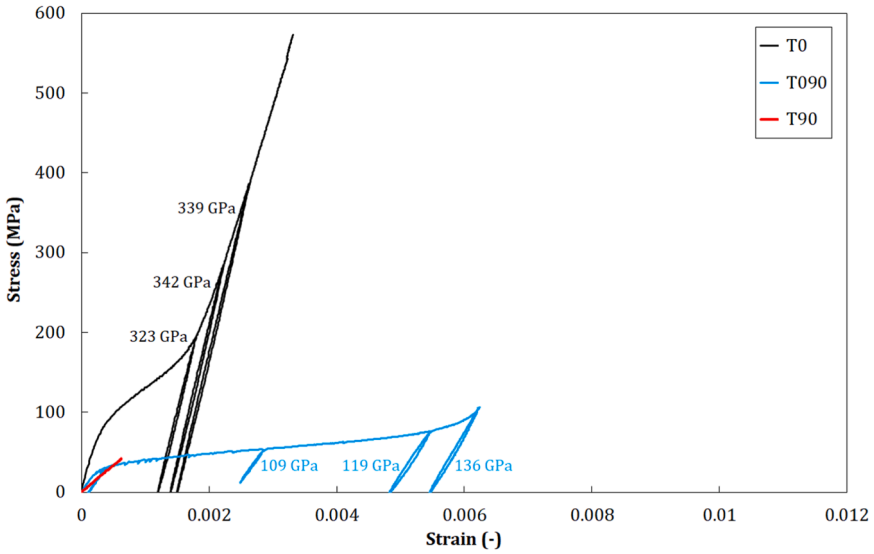

Fig. 3. Representative stress-strain curves of T0, T090 and T90 tensile test. The slopes of the loading/unloading curves are reported in figure.

the matrix, perpendicular to the fiber axis, along with RTS that can be significantly intensified through enhanced matrix densification and strong matrix/fiber interfaces [21,22,38–41]. Table 2

3. Experimental results

Experimental results are reported in Table 3, while representative stress-strain curves of T0, T090 and T90 tensile test are presented in Fig. 3. Curves showed a good repeatability in terms of trend and failure stress and strain. Furthermore, the T090 specimens exhibited strength values comparable to those previously observed in a nominally identical composite demonstrating the process's repeatability and reliability [22]. Conversely, T0 specimens showed unexpectedly high strength value, as evidenced by the ratio of strength values ($\sigma_{0°/0°}/\sigma_{0°/90°} = 568MPa/121MPa = 4.7$). T0 specimens showed the expected peculiar behavior, in which a very stiff elastic behavior in the first range of applied strain ($E_I = 272GPa$), followed by a linear strain-softening plateau with reduced tangent modulus ($E_{II} = 63GPa$). It must be noted that both tangent moduli are smaller than the elastic modulus of the fibers, weighted on their volumetric fraction ($E_f^* = E_f V_f = 780GPa \times 0.45 = 351GPa$). Then, after a certain threshold, a stiffness recovery effect was observed with an increased tangent modulus ($E_{III} = 256GPa$) that reaches values comparable with the one in the first liner part of the curve ($E_{III}/E_I = 0.94$). A similar stiffness recovery ratio was observed in similar UHTCMC during bending [21] and tensile [22] tests. A brittle failure was observed with a sudden and complete loss of load bearing capability. As expected by the "springs' theory", loading/unloading curves showed large residual deformation and the slopes of the unloading curves, obtained after the plateau, are larger that E_I (about 340 GPa *vs.* 272 GPa) and closer to the elastic modulus of the fibers, weighted on their elastic fraction [29].

The permanent deformation and the load plateau are typical of plastic and pseudo-plastic materials, even if it is worth nothing that they were observed on a specimen with an orientation dominated by the fibers, which notoriously have an elastic behavior. The same features were observed in T090 specimens, which exhibit a significantly longer plateau, though the final stiffness recovery is extended for a lower deformation range, thus leading to a significantly lower value of ultimate strength. The yielding stress at the end of the first elastic part [21] was lower than that of T0 specimens. As previously observed [22], the linear strain-softening plateau is larger than the T0, thus causing larger residual deformations, while a shorter strain hardening was observed, bringing rapidly to the failure of the specimen. In this case, the slope of unloading curve is closer to the elastic one and the failure happened brittlely and closer to the plateau. The specimens T90, which behavior is dominated by the matrix, showed a very low strength value and a brittle behavior, with strains at failure that are of an order of magnitude lower than the other kinds of specimen. A higher scattering is present in the failure strength and strain data, typical of statistical materials like ceramics. Considering that both the ZrB_2/SiC matrix and the carbon fibers typically show an elastic behavior up to the failure, the pseudo-plasticity observed could be addressed to the interaction of the two phases, which are subjected to significant RTS at the beginning of the mechanical loading [21,27,28]. The next sections of the paper will delve into such aspect to propose a quantitative model to explain both the pseudo-plastic plateau and the stiffness recovery observed in the responses, in agreement with the observation proposed in [21,28,29].

4. Development of a simplified analytical model

Considering the ultra-high temperature reached during the forming process and the difference in the CTEs [29], it reasonable to suppose the presence of severe RTS, as also reported in literature[42–45], with a tensile stress of state in the matrix phase of about 600 MPa [21] and a compressive one in the fibers that depends on fiber architecture [22].

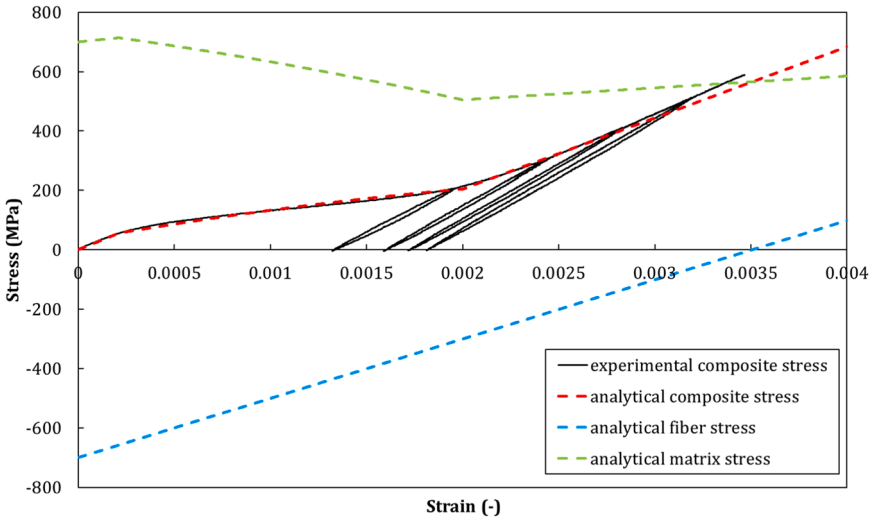

Fig. 4. Comparison between the experimental T0 tensile curve and the curves of the composite, matrix, and fibers stress, obtained by the analytical approach illustrated above.

From these evidences and the observations carried out in [21,22,28,29], an analytical model was developed by applying a simple analytical approach, where the pseudo-plastic phenomena are related to the presence of RTS and to development of matrix damage.

The response of the composite in the direction of the fiber reinforcement and the interaction between the fiber and the matrix can be studied by using a simplified unidimensional micromechanical model, based on the assumption of identical strain, ε, in the fibers and matrix phases (i.e. iso-strain condition). Being E the Young moduli, V the volumetric fraction, and the c, m, f subscripts referred to the composite, the matrix, and the fibers respectively, the stress in the composite material can be expressed with a rule of mixture, as indicated in Eq. (2):

$$\sigma_c = V_f\sigma_f + V_m\sigma_m = s_f + s_m \tag{2}$$

Where s_f and s_m represent the contributions to the stress in the composite provided by fiber phase and the matrix phase. These contributions include the RTSs developed during the manufacturing, compression of the fibers and tension of the matrix, which constitute a self-equilibrating stress state.

The main objective of this simplified model is to corroborate that a strain-softening response attributed to the matrix and the presence of RTSs can explain both the pseudo-plastic plateau and the stiffness recovery obtained in the experimental tests in T0 specimens, still maintaining a perfectly linear elastic response for the fiber. Hence, the stress s_f and the stress increment ds_f for a strain increment $d\varepsilon$ at fixed temperature can be expressed as:

$$s_f = V_f\sigma_f^{RTS} + \widetilde{E}_f\varepsilon \tag{3}$$

$$ds_f = \widetilde{E}_f d\varepsilon \tag{4}$$

Where $\widetilde{E}_f = V_f E_f$ is the effective elastic modulus of the fiber phase in the reinforcement direction. The matrix phase is also subjected to significant RTSs and could have already developed damages since the manufacturing step. However, when a mechanical elongation is imposed to the composite, the matrix phase undergoes a further degradation, being subjected to the coupled action of the residual stress state and the stress originated by the mechanical loading. In the simplified model, such degradation can be represented by introducing a dependence of the matrix elastic modulus on the applied elongation, according to the following expression.

$$\widetilde{E}_m = \widetilde{E}_m(\varepsilon) \tag{5}$$

where $\widetilde{E}_m$ is the secant Young's modulus of the matrix phase (that is the matrix modulus weighted by the corresponding matrix volumetric fraction). Considering Eq. (5), the stress s_m and the stress increment ds_m for a strain increment $d\varepsilon$ can be expressed as:

$$s_m = V_m\sigma_m^{RTS} + \widetilde{E}_m(\varepsilon)\cdot\varepsilon \tag{6}$$

$$ds_m = \widetilde{E}_m^t(\varepsilon)\cdot d\varepsilon \tag{7}$$

Where $\widetilde{E}_m^t = ds_m/d\varepsilon$ is the tangent modulus of matrix phase, which link the increment of mechanical stress to applied elongation. Thus, assuming a linear elastic behavior of the fiber phase, the increment of stress in the composite can be written as:

$$d\sigma_c = E_c^t d\varepsilon = \widetilde{E}_f\cdot d\varepsilon + \widetilde{E}_m^t(\varepsilon)\cdot d\varepsilon \tag{8}$$

$$E_c^t = \widetilde{E}_f + \widetilde{E}_m^t(\varepsilon) \tag{9}$$

From Eq. 9, it can be deduced that if the tangent modulus of the matrix phase evolves and becomes negative, the tangent modulus of the composite can be lower than the fibers stiffness contribution.

$$\widetilde{E}_m^t(\varepsilon) < 0 \Rightarrow E_c^t < \widetilde{E}_f \tag{10}$$

In the limit case a $E_c^t = 0$, that is a perfectly horizontal plateau can be obtained when the negative slope of the matrix phase undergoing strain-softening matches the stiffness of the fiber phase:

$$\widetilde{E}_m^t(\varepsilon) = -\widetilde{E}_f \tag{11}$$

This formulation makes explicit the influence of the volume fraction of the fiber phase on the tangent modulus of the composite during the release of RTSs, which decreases for decreasing volume fractions. This effect could explain the lower tangent modulus observed in the plateau of the tensile curves of T090 specimens.

From the quantitative point of view, the analytical model was used to reconstruct the behavior of the T0 tensile curve, as shown in Fig. 4. The plot was obtained by attributing to $\widetilde{E}_{m0}$ and to $\widetilde{E}_f$ reasonable values, which were evaluated through the decomposition procedure that will be explained in detail in the following Section 4.1. The trend of the tangent modulus of the matrix was shaped considering that the mechanical deformation beyond a certain threshold activates the onset of a damage mechanism that leads to a strain softening regime with a negative tangent modulus. In the physical interpretation of the phenomenon

[21], such damage evolution is promoted by the combined effect stress exerted by fibers, which are compressed due to the presence of RTSs and by the additional stress induced by the applied elongation. As this RTS state is relaxed, due to the increasing elongation, also the total stress acting in the matrix is reduced and the damage mechanisms in the matrix are arrested, ending the softening regime. Consequently, the strain-softening regime in the matrix phase is terminated, the compressed fibers are no more able to elongate against the matrix resistance. Consequently, the stiffness of the material is recovered in the final portion of the response [21]. For this simplified rheological unidimensional model, a hypothetical very simple matrix response was calibrated so to match the response of the [0] tensile test. The response obtained is represented by the dashed green line reported in Fig. 4, while the response of the fiber is considered linear elastic as represented be the blue dashed lines in Fig. 4. The response of the composite according to the analytical model shows that the proposed interpretation can explain the trend of the overall nonlinear curve, as evidenced in Fig. 4.

If the dependence of the tangent modulus of the matrix phase on the elongation can be modelled by damage mechanics, the following relation can be written, introducing a scalar damage factor $D(\varepsilon)$:

$$\widetilde{E}_m(\varepsilon) = (1 - D(\varepsilon))\cdot\widetilde{E}_m^0 \tag{12}$$

Where $\widetilde{E}_m^0$ is the initial elastic modulus of the matrix phase at the end of the manufacturing. Then, the increment of the stress in the matrix phase can be written as:

$$d\sigma_m = \widetilde{E}_m(\varepsilon)\cdot d\varepsilon + d\widetilde{E}_m(\varepsilon)\cdot\varepsilon = \left(\widetilde{E}_m(\varepsilon) + \frac{d\widetilde{E}_m(\varepsilon)}{d\varepsilon}\varepsilon\right)d\varepsilon = \widetilde{E}_m^t(\varepsilon)\cdot d\varepsilon \tag{13}$$

In the frame of damage mechanics, by using Eq. 12, the relationship between the tangent and the secant modulus can be written as in Eq. 14:

$$\widetilde{E}_m^t(\varepsilon) = \widetilde{E}_m(\varepsilon) + \frac{d\widetilde{E}_m(\varepsilon)}{d\varepsilon}\varepsilon = \widetilde{E}_m(\varepsilon) - \frac{dD(\varepsilon)}{d\varepsilon}\widetilde{E}_m^0\cdot\varepsilon \tag{14}$$

Although Eq. 14 can be used to evaluate a hypothetical damage evolution law in the matrix, it must be remarked that the model presented so far is unidimensional and tailored to capture only the response of T0 specimens. Moreover, damage mechanics cannot explain the permanent residual deformation obtained in the experiments. A more detailed and complete model, also including plasticity, was developed, and implemented in a finite element code, with the aim of capturing the nonlinearities of both the [0] and the [0/90] coupons, including deviation from linearity, the plateaus, and final stiffness recovery.

5. Bi-phasic finite element model

A mesoscale finite element model was set up with the aim of validating the interpretation of the nonlinear behavior of the UHTCMC based on the presence of RTS, presented in Section 3. The model must be capable of capturing those behaviors both for T0 and T090 specimens. T90 specimens showed a matrix-dominated behavior, perfectly elastic and brittle not related with RTS, so their modelling was not included in this work. The model was implemented in SIMULIA Abaqus/Explicit code on a representative geometry of few elements.

Table 4
Input data used for numerical modelling, where E_{ij} are the elastic moduli, G_{ij} are the shear moduli, and υ_{ij} are the Poisson's ratios. Transversal isotropy was assumed such as $E_{22} = E_{33}$ and $\upsilon_{12} = \upsilon_{13}$. For sake of simplicity, $G_{12} = G_{23} = G_{31}$ was assumed.

Property		Source
E_{11}	272*GPa*	*Tensile tests of T0specimens*
$E_{22} = E_{33}$	74*GPa*	*Tensile tests of T90specimens*
$\upsilon_{12} = \upsilon_{13}$	0.1	*Tensile tests*

Table 5
Decomposed elastic properties for a 0° oriented ply in T0 and T090 composite.

	0° oriented ply in T0	0° oriented ply in T090
Idealized fibers phase stiffness matrix	$D^f =$ $\begin{pmatrix} 198556 & 0 & 0 \\ 0 & 0 & 0 \\ 0 & 0 & 0 \end{pmatrix} MPa$	$D^f =$ $\begin{pmatrix} 163152 & 0 & 0 \\ 0 & 0 & 0 \\ 0 & 0 & 0 \end{pmatrix} MPa$
Idealized matrix phase Young's modulus	73783*MPa*	73783*MPa*
Idealized matrix phase Poisson's ratio	0.082	0.082

5.1. Material decomposition and superimposed mesh

Mesoscale bi-phasic approaches proved to be a stable and reliable tool for the simulation and prediction of both in-plane and out-of-plane nonlinear behavior of fiber reinforced composite materials [30,33,34]. They are based on the separation of the composite properties in two different idealized phases. The first one is the idealized fibers phase, which represents the continuity of the reinforcement and carries stress only in the reinforcement direction. The second one is the idealized matrix phase, which is an equivalent medium that represents the matrix-dominated behavior of the composite [30,33,34]. A bi-phasic approach was used for the material studied in this work, based on the formulation presented in Airoldi et al. [34]. In that case, the two idealized phases are superimposed and share the same volume. For a unidirectional composite, the elastic constitutive law results in Eq. 17, where D_{ij} are the components of the stiffness matrix and the apexes f and m stand for idealized fiber and matrix phase respectively.

$$\begin{bmatrix} \sigma_{11} \\ \sigma_{22} \\ \sigma_{33} \\ \tau_{12} \\ \tau_{23} \\ \tau_{31} \end{bmatrix} = \left(\begin{bmatrix} V_f E_f & 0 & 0 & 0 & 0 & 0 \\ 0 & 0 & 0 & 0 & 0 & 0 \\ 0 & 0 & 0 & 0 & 0 & 0 \\ 0 & 0 & 0 & 0 & 0 & 0 \\ 0 & 0 & 0 & 0 & 0 & 0 \\ 0 & 0 & 0 & 0 & 0 & 0 \end{bmatrix} + \begin{bmatrix} D_{11}^m & D_{12}^m & D_{13}^m & 0 & 0 & 0 \\ D_{21}^m & D_{22}^m & D_{23}^m & 0 & 0 & 0 \\ D_{31}^m & D_{32}^m & D_{33}^m & 0 & 0 & 0 \\ 0 & 0 & 0 & D_{44}^m & 0 & 0 \\ 0 & 0 & 0 & 0 & D_{55}^m & 0 \\ 0 & 0 & 0 & 0 & 0 & D_{66}^m \end{bmatrix} \right) \begin{bmatrix} \varepsilon_{11} \\ \varepsilon_{22} \\ \varepsilon_{33} \\ \gamma_{12} \\ \gamma_{23} \\ \gamma_{31} \end{bmatrix} \tag{17}$$

To obtain the properties of the two idealized phases, a decomposition algorithm was used, which is widely described in Ref.[34]. In the application to the UHTCMC materials studied in this paper, the

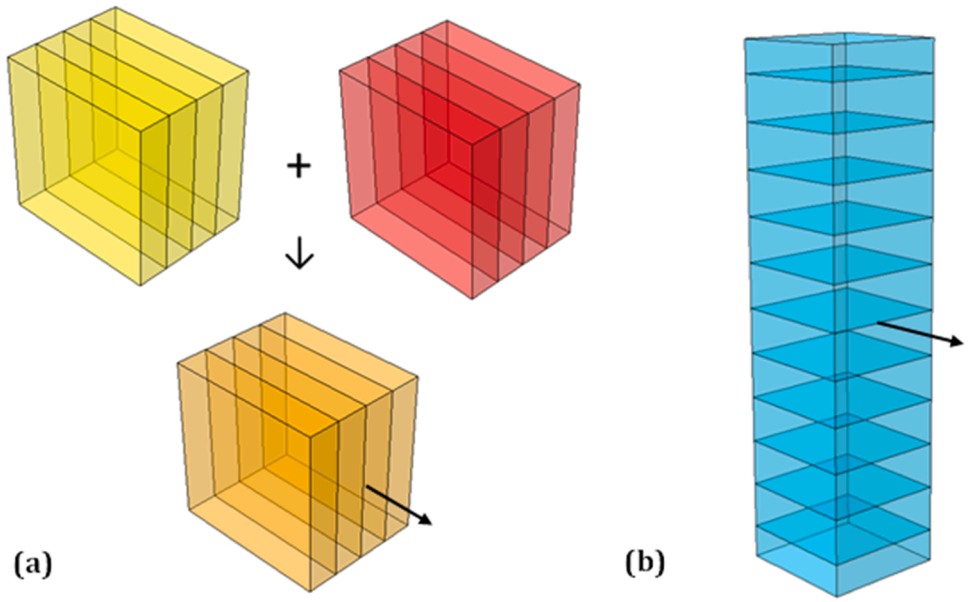

Fig. 5. Superimposed meshes of (a) T0 specimen and (b) T090 specimen. Pulling direction is evidenced by black arrows. Superimposed meshes are composed of two layers of C3D8R elements that share the same nodes.

algorithm was adapted to obtain an isotropic idealized matrix phase. The input data for the decomposition algorithm are reported in Table 4.

However, the different characteristics of the plies in T0 and T090 specimens, discussed in Section 2.3, required two different evaluations of the fiber phase stiffness $V_f E_f$, to represent the fiber contribution in both T0 and T090 specimens. In agreement with the morphological differences observed between T0 and T090 specimens, the stiffness of the T090 fiber phase $V_f E_f$ was obtained by reducing the one of T0, making a series of assumptions based on the evidence described in Section 2.3. The difference of compaction of the plies gives reason for a reduction of fibers volumetric fraction in T090 of about 10%. Additionally, the other morphological differences (outer plies thickness, porosity, …) makes possible considering a further reduction of about 8%, so that a final reduction of 17.8% was assumed to match the elastic properties of both T0 and T090 with the same isotropic matrix and different fiber contributions. Table 5

5.2. FEM implementation

The bi-phasic model described was implemented in two different FEM models inside the SIMULIA Abaqus/Standard environment, to simulate the tensile behavior of T0 and T090 specimens. As already mentioned, material decomposition allows to define two idealized phases that share the same volume. For this reason, the mesh of each model is composed of two layers of C3D8R solid elements that are superimposed, sharing the same nodes: a layer represents the fiber, characterized with an orthotropic elastic material model available in the solver code, and the other one representing the idealized matrix, which was characterized by developing a user material subroutine (VUMAT) described in the next sections. Only representative elements of the laminates were developed, avoiding unnecessary computational costs and the complications inherent to the simulation of RTSs build-up with models including the tabs.

For the T0 model, a geometry with dimensions $L1mm \times W1mm \times T0.8mm$, meshed with two superimposed sets composed by four elements, was used. For the T090 model, a geometry with dimensions $L1mm \times W1mm \times T4mm$, meshed with two superimposed sets composed by twelve elements, was used. It should be observed that the thickness of the external elements is smaller than the one of the internal elements, to respect the original proportion of the T090 specimens (see Section 2.3). The two meshes are shown in Fig. 5.

The two surfaces normal to the pulling direction were constrained to two reference points using an equation that allows the transversal movement of the nodes. A two-step analysis was defined: the first step to simulate the temperature decrease after the forming process and the second one to simulate the tensile test. It is important to underline that both are stress-displacement steps, heat transfer is not included, and temperature have effects only by means of CTEs. In the first step, the left reference point was constrained to forbid any displacement, while the right one was allowed to translate only along the x direction. In this way, the specimen is allowed to shrink when a smoothed ramp of temperature with magnitude $\Delta T = -1500°C$ was applied to all the nodes [29]. Due to the CTEs mismatch the superimposed elements generate different thermal strains, but since they share the same nodes, they cannot shrink freely. In this way, RTSs are generated inside the elements. In the second step, the same constraints at the reference points were used, but in addition an imposed velocity was applied the right reference point. Two sections were defined for the two materials using the decomposed material properties, one orthotropic for the idealized fibers phase and one isotropic for the idealized matrix phase. Fiber material model includes only the elastic behavior, while for matrix material a nonlinear constitutive law was defined.

5.3. Matrix constitutive law

From the results of the experimental characterization, the UHTCMC showed a pseudo-plastic behavior with large deviation from linearity and permanent deformations. Given this evidence, a constitutive law based on the theory of plasticity was chosen. Additionally, the onset of a strain softening regime was required to activate the release of the RTSs in the fibers, as shown by the analytical model described in section 4.1. Hence, an orthotropic ductile damage law was implemented, to represent the orthotropic material degradation. This constitutive law was implemented in a custom routine inside the Simulia/Abaqus Explicit environment.

5.3.1. Drucker-Prager plasticity

Among the different plastic yielding theory, Von Mises yielding criterion is the simplest, but it cannot capture the yielding points of both T0

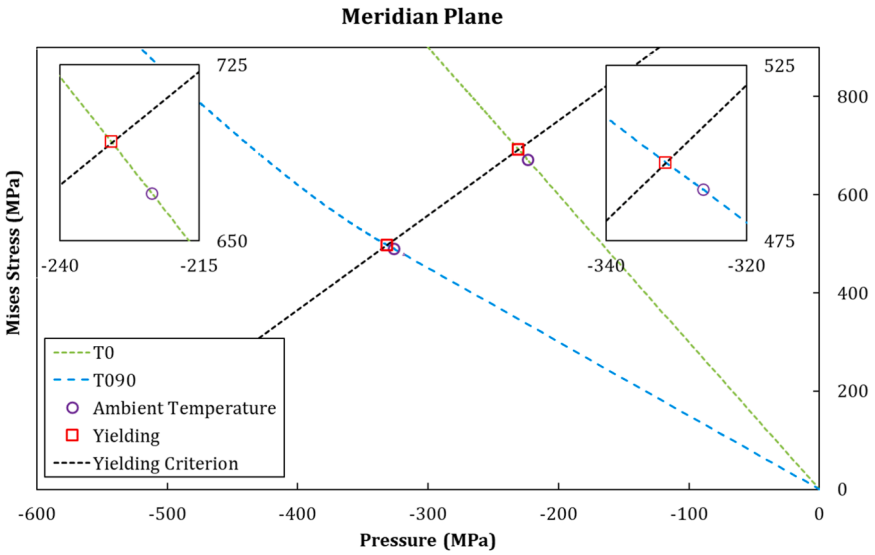

Fig. 6. Elastic response of the state of stress of T0 and T090 during the cooling phase and pulling phase in the meridian plane. The purple circles represent the state of stress when ambient temperature is reached, while the red rhombuses represent the yielding stress state.

and T090, because the one of T0 is significantly higher than the one of T090. Considering that RTSs develop in the fiber direction, the RTSs in the idealized matrices phases of T0 and T090 differ considerably. In fact, in T0 RTSs are present in the 0° direction only, while in T090 they are present both in 0° and 90° directions. This biaxial state of stress of T090 significatively increased the hydrostatic component of the stress tensor, making it significatively higher than the one of T0. So, a law capable of distinguishing a different yielding value for different pressure stress state was needed. The Drucker-Prager yielding criterion is the pressure dependent version of the Von Mises criterion and it has been already used in literature for similar applications [33]. It was implemented in the form:

$$\sigma_{Mises} = \tan\theta \cdot p + d \tag{18}$$

Where the first component is the Mises stress, that represent the deviatoric part of the stress tensor, and is defined, as show in Eq. 19, p is the pressure stress defined as the negative of the hydrostatic part of the stress tensor, θ is the friction angle and d is the cohesion term.

$$\sigma_{Mises} = \sqrt{0.75 J_2} \tag{19}$$

Where J_2 is the second invariant of the deviatoric stress tensor. In this law the evolution of the internal variables, i.e. the hardening curve, is represented by the cohesion term that evolves with the plastic equivalent strain. This equivalent acts as a scalar index of the amount of plastic strain and is obtained by integrating in time the plastic equivalent strain rate defined as shown in Eq. 20.

$$\dot{\bar{\varepsilon}}^{pl} = \sqrt{\frac{2}{3}\dot{\varepsilon}_{ij}^{pl} \cdot \dot{\varepsilon}_{ij}^{pl}} \tag{20}$$

5.3.2. Orthotropic damage

An orthotropic damage law was defined on top of the yielding criterion to represent the loss of load bearing capability that depends on the orientation of the material. In coherence with the choice of an elasto-plastic model, a ductile damage law was chosen, in which the different directional components of damage, which in this case are d_{11} and d_{22}, depend on the directional components of the plastic strain. Moreover, experimental evidence showed that in T090, in which a strong biaxial stress is present, the damage seems to be amplified with respect to T0. For this reason, a dependence of the damage from the biaxiality ξ was included. The biaxiality was expressed as:

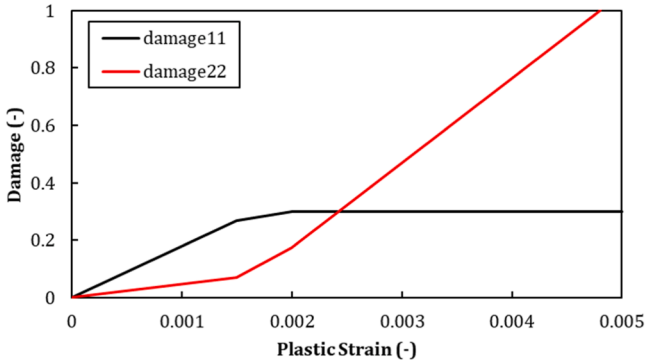

Fig. 7. Final curves of damage components dependent on directional components of plastic strain.

$$\xi = \frac{\sigma_{22}}{\sigma_{11}} \tag{21}$$

The final formulation of the damage law is shown in Eq. 23, where biaxiality acts as an amplifier of the damage.

$$d_{ij} = (1 + A \bullet \xi) \bullet f\left(\varepsilon_{ij}^{pl}\right) \tag{22}$$

Where the damage functions f were defined in a tabular way and A a material constant. The damage directly affects the effective stress by degrading the undamaged or trial stress tensor, as shown in Eq. 24.

$$\sigma_{ij} = \left(1 - d_{ij}\right) \bullet \sigma_{ij}^{trial} \tag{23}$$

5.4. Model calibration

A was set for the fibers phase, while a $CTE = 8.3 \bullet 10^{-6}\ \ ^{\circ}C^{-1}$ was set for the idealized matrix phase. It is important to underline that these CTEs were set constant using a value measured at room temperature, thus the RTSs amount obtained approximates the real one but remaining in line with the literature value [21]. To tune the Drucker-Prager yielding criterion, preliminary linear analyses were carried out and

the history of the elastic response in the idealized matrix phase of both T0 and T090 was plotted into the meridian plane, defined by the pressure, the inverse of the volumetric stress, on the abscissa and the

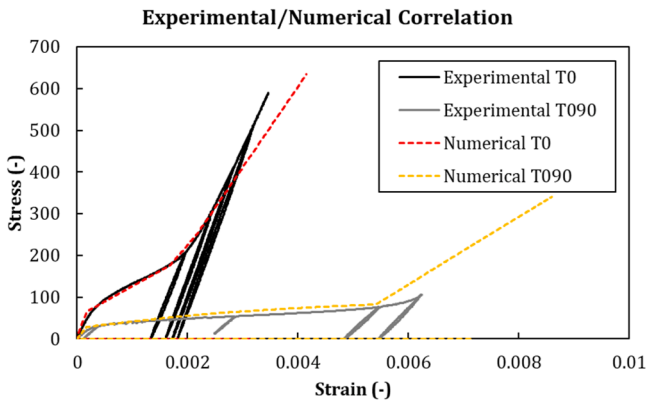

Fig. 8. Comparison between numerical and experimental tensile curves of specimen T0 and T090. The first part of the curves where the specimens are strained without stress corresponds to the cooling phase of the simulations.

Mises stress on the ordinate, as shown in Fig. 6. At time zero, after the forming phase, the composite is completely unstressed. During the cool down phase, RTSs start increasing with two different slopes since the T090 has a bigger pressure component. It is worth noting that the calibration lead to the difference between the RTS at RT and the yielding stress of just a few tens of megapascals as experimentally observed in [21]. At points corresponding to the circles in Fig. 6, the specimens reached room temperature at the end of the cooling step, and they started to be pulled in the simulation of mechanical loading. At points corresponding to the rhombuses in Fig. 6, the specimens reached the experimental yielding point in the simulation of mechanical loading. The Drucker-Prager criterion must intercept both these two yielding points. Hence, a friction angle of 20° and a cohesion of 548 MPa were selected. Thereafter, tabular damage functions and the A constant in the damage laws (Eq. 22) were tuned with a trial-and-error process to capture the softening plateau and the sequent hardening of both T0 and T090. The two tuned damage functions for $\xi = 0$ are shown in Fig. 7. Hence, while the damage along fiber direction reaches a kind of saturation, the damage in the transverse direction increases continuously. Despite the simplification involved in the presented model, such behavior is reasonable.

5.5. Numerical-experimental correlation

The correlation between experimental and numerical curves obtained with the calibrated models are shown in Fig. 8. The numerical curves capture with a good approximation the trend of the two curves except for the strain-hardening part of the T0 curves, that is underestimated of about 15%. This error is due to the damage introduced to represent the strain-softening regimen of the matrix, which lowers the stiffness of the matrix, causing a reduction of the elastic properties of the whole composite when the stiffness is recovered. Loading/unloading cycles were also performed to show the capability of the model to capture the residual deformations with a small error due to the same reason as above. In Fig. 9, the capability of the model to qualitatively capture the dependence on ΔT of the cooling phase, thus the RTS, of the nonlinearities are shown. The yielding points progressively increase with higher temperature, and consequently the strain-hardening is delayed, in line with the experimental observations of Ref.s [21,22,46].

6. Conclusions

In this work, the nonlinear response of a unidirectional $C_f - ZrB_2/SiC$ UHTCMC produced by slurry infiltration and SPS, evidenced by a campaign of tensile tests on unidirectional and cross-ply specimens, was characterized and modelled.

Quantitative models were developed assuming, in agreement with experimental observations and interpretations carried out in previous works, that the observed non-linear trends in the direction of fiber reinforcement were related to the interaction between the RTSs in the material at the end of the manufacturing and the degradation of the material surrounding the fibers, which lose the capability to keep the fiber in highly compressed stress state.

The development of such models at the meso-scale, without the detailed reconstruction of the microstructure of the material, required the adoption of a bi-phasic point of view, based on the definition of idealized fiber and matrix phases. An analytical model indicated that the introduction of a strain-softening regime in the matrix response could capture the yielding, the plateau, and the final stiffness recovery and provided the analytical conditions to obtain such responses. The representation of the response both for unidirectional and cross-ply lamination sequences required the consideration of the different types of RTS states in the two cases, which led to model the matrix with a pressure-

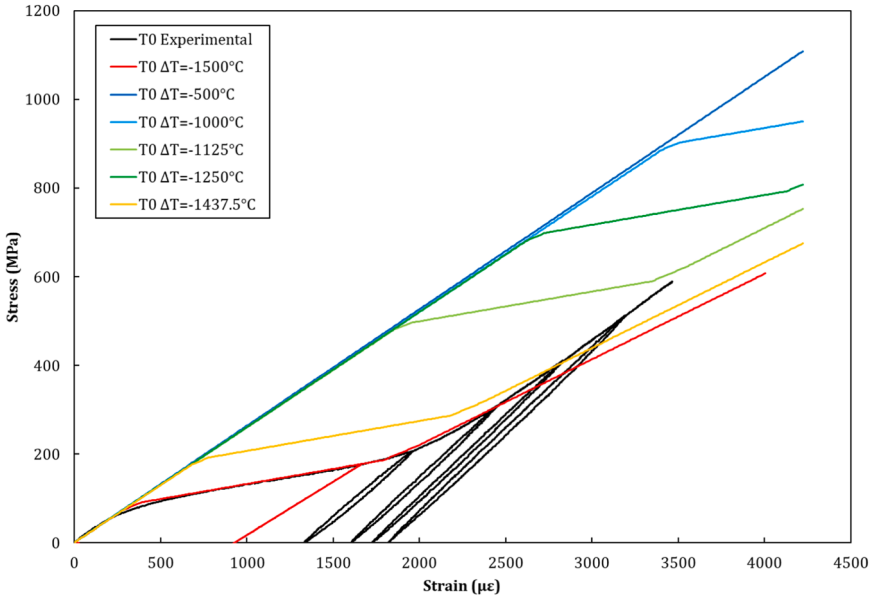

Fig. 9. Temperature dependence of the numerical model. At decreasing ΔT the nonlinearities shift towards higher strain values, thus disappearing.

dependent yield criterion and an associated plastic flow. Damage evolution in the idealized matrix material was tuned to capture the yield stress, the slope in the plateau region, the extension of the plateau, and, with small discrepancy, the slope in the final phase of stiffness recovery in both the lay-ups.

Such results confirm the validity of the qualitative interpretations provided in previous works and define the bases for a further development and implementation of constitutive models that could be used at the macroscale for the design of parts with UHTCMCs having significant structural roles.

CRediT authorship contribution statement

Antonio Maria Caporale: Conceptualization, Methodology, Software, Investigation, Data curation, Writing – original draft, Visualization, Writing – review & editing. **Pietro Galizia**: Conceptualization, Methodology, Software, Formal analysis, Investigation, Data curation, Writing – original draft, Visualization, Writing – review & editing, Project administration. **Bartolomeo Zanardi**: Methodology, Software. **Antonio Vinci**: Resources. **Diletta Sciti**: Resources, Funding acquisition, Project administration, Writing – review & editing. **Alessandro Airoldi**: Conceptualization, Methodology, Formal analysis, Writing – review & editing, Supervision, Project administration, Funding acquisition.

Declaration of Competing Interest

The authors declare that they have no known competing financial interests or personal relationships that could have appeared to influence the work reported in this paper.

Acknowledgements

This work was supported by the Italian Space Agency (ASI) as part of the project AM3aC2A: Multi-scale approach for modelling CMC and UHTCMC materials.

References

[1] S. Mungiguerra, L. Silvestroni, R. Savino, L. Zoli, B. Esser, M. Lagos, D. Sciti, Qualification and reusability of long and short fibre-reinforced ultra-refractory composites for aerospace thermal protection systems, Corros. Sci. 195 (2022) 109955.

[2] N.T. Drenthe, B.T.C. Zandbergen, R. Curran, M.O. Van Pelt, Cost estimating of commercial smallsat launch vehicles, Acta Astronaut 155 (2019) 160–169, https://doi.org/10.1016/J.ACTAASTRO.2018.11.054.

[3] H. Hald, Operational limits for reusable space transportation systems due to physical boundaries of C/SiC materials, Aerosp. Sci. Technol. 7 (2003) 551–559, https://doi.org/10.1016/S1270-9638(03)00054-3.

[4] W.J. Li, D.Y. Cheng, X.G. Liu, Y.B. Wang, W.H. Shi, Z.X. Tang, F. Gao, F.M. Zeng, H. Y. Chai, W.B. Luo, Q. Cong, Z.L. Gao, On-orbit service (OOS) of spacecraft: A review of engineering developments, Prog. Aerosp. Sci. 108 (2019) 32–120, https://doi.org/10.1016/j.paerosci.2019.01.004.

[5] A.R. Mishra, S. Vajinder, M. Patel, R. Mitra, 3D microstructure characterization of 2D Cf-ZrB2-SiC ultra-high temperature ceramic matrix composites using X-ray microscopy, Ceram. Int. 50 (2024) 4492–4501, https://doi.org/10.1016/j.ceramint.2023.11.183.

[6] Y. Liu, J. Wang, R. Jing, Y. Zhang, Z. Liao, Y. Zu, Enhanced fracture properties of continuous Cf/ZrB2-based composites with polydopamine-derived carbon boundary layer, Surf. Interfaces 46 (2024) 103925, https://doi.org/10.1016/j.surfin.2024.103925.

[7] P. Galizia, S. Failla, C. Melandri, D. Sciti, Local indentation response of carbon fibers embedded in a harsh environment: The sintered ultra-high temperature ceramic matrix, J. Eur. Ceram. Soc. (2023), https://doi.org/10.1016/j.jeurceramsoc.2023.12.025.

[8] Y. Cheng, F. Zhang, D. Ma, Y. Zhang, Y. Liu, Y. An, A. Wang, N. Hu, L. Zhao, W. Han, Long-term oxidation and ablation behavior of Cf/ZrB2–SiC composites at 1500, 2000, and 2200°C, Int. J. Appl. Ceram. Technol. 20 (2023) 1636–1645, https://doi.org/10.1111/IJAC.14299.

[9] Z. Wang, B. Wang, S. Li, X. Jin, X. Zhang, S. Meng, G. Fang, Temperature-dependent oxidation kinetics and mechanical properties degradation of Cf/ZrB2-SiC composites, Corros. Sci. (2023) 111479, https://doi.org/10.1016/j.corsci.2023.111479.

[10] C. Fang, Y. Bao, P. Hu, S. Dong, D. Liu, H. Wang, X. Zhang, Effects of multilayer hydrothermal carbon interphases on mechanical properties and thermal shock resistance of CF/ZrB2-SiCBN, J. Eur. Ceram. Soc. 42 (2022) 4759–4769, https://doi.org/10.1016/j.jeurceramsoc.2022.05.029.

[11] T. Marumo, N. Koide, Y. Arai, T. Nishimura, M. Hasegawa, R. Inoue, Characterization of carbon fiber-reinforced ultra-high temperature ceramic matrix composites fabricated via Zr-Ti alloy melt infiltration, J. Eur. Ceram. Soc. 42 (2022) 5208–5219, https://doi.org/10.1016/j.jeurceramsoc.2022.06.040.

[12] D. Sciti, L. Zoli, T. Reimer, A. Vinci, P. Galizia, A systematic approach for horizontal and vertical scale up of sintered Ultra-High Temperature Ceramic Matrix Composites for aerospace – Advances and perspectives, Compos. Part B Eng. 234 (2022) 109709, https://doi.org/10.1016/J.COMPOSITESB.2022.109709.

[13] P. Galizia, A. Vinci, L. Zoli, F. Monteverde, J. Binner, V. Venkatachalam, M. A. Lagos, T. Reimer, N. Jain, D. Sciti, Retained strength of UHTCMCs after oxidation at 2278 K, Compos. Part A Appl. Sci. Manuf. 149 (2021) 106523, https://doi.org/10.1016/j.compositesa.2021.106523.

[14] P. Galizia, D. Sciti, N. Jain, Insight into microstructure and flexural strength of ultra-high temperature ceramics enriched SICARBON™ composite, Mater. Des. (2021) 109888, https://doi.org/10.1016/j.matdes.2021.109888.

[15] D. Zhang, H. Yu, A. Wang, P. Hu, L. Ren, D. Sun, Ablation behavior and mechanisms of 3D Cf/ZrB2-SiC composite applied in long-term temperature up to 2400 °C, Corros. Sci. 190 (2021) 109706, https://doi.org/10.1016/J.CORSCI.2021.109706.

[16] D. Ni, Y. Cheng, J. Zhang, J.-X. Liu, J. Zou, B. Chen, H. Wu, H. Li, S. Dong, J. Han, X. Zhang, Q. Fu, G.-J. Zhang, Advances in ultra-high temperature ceramics, composites, and coatings, J. Adv. Ceram. 111 (11) (2021) 1–56, https://doi.org/10.1007/S40145-021-0550-6.

[17] J. Binner, M. Porter, B. Baker, J. Zou, V. Venkatachalam, V.R. Diaz, A. D'Angio, P. Ramanujam, T. Zhang, T.S.R.C. Murthy, Selection, processing, properties and applications of ultra-high temperature ceramic matrix composites, UHTCMCs–a review, Int. Mater. Rev. 65 (2020) 389–444, https://doi.org/10.1080/09506608.2019.1652006.

[18] L.M. Rueschhoff, C.M. Carney, Z.D. Apostolov, M.K. Cinibulk, Processing of fiber-reinforced ultra-high temperature ceramic composites: a review, Int. J. Ceram. Eng. Sci. 2 (2020) 22–37, https://doi.org/10.1002/ces2.10033.

[19] B.W. Chen, D.W. Ni, C.J. Liao, Y.L. Jiang, J. Lu, S.M. Dong, Long-term ablation behavior and mechanisms of 2D-Cf/ZrB2-SiC composites at temperatures up to 2400 °C, Corros. Sci. 177 (2020) 108967, https://doi.org/10.1016/J.CORSCI.2020.108967.

[20] D. Zhang, P. Hu, S. Dong, X. Liu, C. Wang, Z. Zhang, X. Zhang, Oxidation behavior and ablation mechanism of Cf/ZrB2-SiC composite fabricated by vibration-assisted slurry impregnation combined with low-temperature hot pressing, Corros. Sci. 161 (2019) 108181, https://doi.org/10.1016/j.corsci.2019.108181.

[21] P. Galizia, D. Sciti, Disclosing residual thermal stresses in UHT fibre-reinforced ceramic composites and their effect on mechanical behaviour and damage evolution, Compos. Part B Eng. 248 (2023) 110369, https://doi.org/10.1016/J.COMPOSITESB.2022.110369.

[22] P. Galizia, D. Sciti, J. Binner, V. Venkatachalam, M.A. Lagos, F. Servadei, A. Vinci, L. Zoli, T. Reimer, Elevated temperature tensile and bending strength of ultra-high temperature ceramic matrix composites obtained by different processes, J. Eur. Ceram. Soc. 43 (2023) 4588–4601, https://doi.org/10.1016/j.jeurceramsoc.2023.03.055.

[23] G. Camus, L. Guillaumat, S. Baste, Development of damage in a 2D woven C/SiC composite under mechanical loading: I. Mechanical characterization, Compos. Sci. Technol. 56 (1996) 1363–1372, https://doi.org/10.1016/S0266-3538(96)00094-2.

[24] K.G. Dassios, D.G. Aggelis, E.Z. Kordatos, T.E. Matikas, Cyclic loading of a SiC-fiber reinforced ceramic matrix composite reveals damage mechanisms and thermal residual stress state, Compos. Part A Appl. Sci. Manuf. 44 (2013) 105–113, https://doi.org/10.1016/j.compositesa.2012.06.011.

[25] B.W. Chen, D.W. Ni, C.J. Liao, Y.L. Jiang, J. Lu, Y.S. Ding, H. Da Wang, S.M. Dong, Chemical reactions and thermal stress induced microstructure evolution in 2D-Cf/ZrB2-SiC composites, J. Mater. Sci. Technol. 83 (2021) 75–82, https://doi.org/10.1016/J.JMST.2020.12.054.

[26] D. Sciti, A. Vinci, L. Zoli, P. Galizia, S. Failla, S. Mungiguerra, G.D. Di Martino, A. Cecere, R. Savino, Propulsion tests on ultra-high-temperature ceramic matrix composites for reusable rocket nozzles, J. Adv. Ceram. 12 (2023) 1345–1360, https://doi.org/10.26599/JAC.2023.9220759.

[27] Z. Wang, G. Fang, B. Wang, P. Hu, F. Yi, S. Meng, Study on toughening mechanisms of pyrolytic carbon interface layer in Cf/ZrB2-SiC composites using in-situ tensile experimental and numerical methods, J. Eur. Ceram. Soc. (2021), https://doi.org/10.1016/j.jeurceramsoc.2021.04.028.

[28] P. Galizia, D. Sciti, F. Saraga, L. Zoli, Off-axis damage tolerance of fiber-reinforced composites for aerospace systems, J. Eur. Ceram. Soc. 40 (2020) 2691–2698, https://doi.org/10.1016/j.jeurceramsoc.2019.12.038.

[29] P. Galizia, L. Zoli, D. Sciti, Impact of residual stress on thermal damage accumulation, and Young's modulus of fiber-reinforced ultra-high temperature ceramics, Mater. Des. 160 (2018) 803–809, https://doi.org/10.1016/J.MATDES.2018.10.019.

[30] B.N. Cox, W.C. Carter, N.A. Fleck, A binary model of textile composites—I. Formulation, Acta Metall. Mater. 42 (1994) 3463–3479, https://doi.org/10.1016/0956-7151(94)90479-0.

[31] J. Xu, B.N. Cox, M.A. McGlockton, W.C. Carter, A binary model of textile composites–II. The elastic regime, Acta Metall. Mater. 43 (1995) 3511–3524, https://doi.org/10.1016/0956-7151(95)00057-3.

[32] Q.D. Yang, K.L. Rugg, B.N. Cox, D.B. Marshall, Evaluation of Macroscopic and Local Strains in a Three-Dimensional Woven C/SiC Composite, J. Am. Ceram. Soc. 88 (2005) 719–725, https://doi.org/10.1111/j.1551-2916.2005.00156.x.
[33] S. Flores, A.G. Evans, F.W. Zok, M. Genet, B.N. Cox, D.B. Marshall, O. Sudre, Q. Yang, Treating matrix nonlinearity in the binary model formulation for 3D ceramic composite structures, Compos. Part A Appl. Sci. Manuf. 41 (2010) 222–229, https://doi.org/10.1016/j.compositesa.2009.10.020.
[34] A. Airoldi, C. Mirani, L. Principito, A bi-phasic modelling approach for interlaminar and intralaminar damage in the matrix of composite laminates, Compos. Struct. 234 (2020) 111747, https://doi.org/10.1016/j.compstruct.2019.111747.
[35] L. Zoli, A. Vinci, P. Galizia, C.F. Gutièrrez-Gonzalez, S. Rivera, D. Sciti, Is spark plasma sintering suitable for the densification of continuous carbon fibre - UHTCMCs? J. Eur. Ceram. Soc. 40 (2020) 2597–2603, https://doi.org/10.1016/j.jeurceramsoc.2019.12.004.
[36] D. Sciti, L. Zoli, A. Vinci, L. Silvestroni, S. Mungiguerra, P. Galizia, Effect of PAN-based and pitch-based carbon fibres on microstructure and properties of continuous Cf/ZrB2-SiC UHTCMCs, J. Eur. Ceram. Soc. 41 (2021) 3045–3050, https://doi.org/10.1016/j.jeurceramsoc.2020.05.032.
[37] P. Galizia, S. Failla, L. Zoli, D. Sciti, Tough salami-inspired Cf/ZrB2 UHTCMCs produced by electrophoretic deposition, J. Eur. Ceram. Soc. 38 (2018) 403–409, https://doi.org/10.1016/j.jeurceramsoc.2017.09.047.
[38] D. Xiaolin, D. Zhao, X. Fan, X. Ma, X. Chen, J. Xue, F. Ye, Y. Liu, In-plane thermal expansion behavior of M55J carbon fiber reinforced SiC matrix composite (in press), J. Eur. Ceram. Soc. (2023) (in press).
[39] X. Fan, X. Ma, X. Dang, J. Xue, F. Ye, D. Zhao, L. Cheng, In-plane thermal expansion behavior of dense ceramic matrix composites containing SiBC matrix, J. Eur. Ceram. Soc. 40 (2020) 3414–3422, https://doi.org/10.1016/j.jeurceramsoc.2020.03.006.
[40] H. Mei, Measurement and calculation of thermal residual stress in fiber reinforced ceramic matrix composites, Compos. Sci. Technol. 68 (2008) 3285–3292, https://doi.org/10.1016/j.compscitech.2008.08.015.
[41] K.G. Dassios, T.E. Matikas, Residual stress-related common intersection points in the mechanical behavior of ceramic matrix composites undergoing cyclic loading, Exp. Mech. 53 (2013) 1033–1038, https://doi.org/10.1007/s11340-012-9709-y.
[42] Y. Li, P. Xiao, Z. Li, W. Zhou, T. Liensdorf, W. Freudenberg, F. Reichert, N. Langhof, W. Krenkel, Strength evolution of cyclic loaded LSI-based C/C-SiC composites, Ceram. Int. 42 (2016) 14505–14510, https://doi.org/10.1016/j.ceramint.2016.06.061.
[43] R. Naslain, Fibre-matrix interphases and interfaces in ceramic matrix composites processed by CVI, Compos. Interfaces 1 (1993) 253–286, https://doi.org/10.1163/156855493×00112.
[44] Y. Ding, S. Dong, Q. Zhou, Z. Huang, D. Jiang, Preparation of C/SiC Composites by Hot Pressing, Using Different C Fiber Content as Reinforcement, J. Am. Ceram. Soc. 89 (2006) 1447–1449, https://doi.org/10.1111/j.1551-2916.2005.00872.x.
[45] S. Ochiai, H. Tanaka, S. Kimura, M. Tanaka, M. Hojo, K. Okuda, Modeling of residual stress-induced stress–strain behavior of unidirectional brittle fiber/brittle matrix composite with weak interface, Compos. Sci. Technol. 63 (2003) 1027–1040, https://doi.org/10.1016/S0266-3538(03)00015-0.
[46] L. Zoli, A. Vinci, P. Galizia, C. Melandri, D. Sciti, On the thermal shock resistance and mechanical properties of novel unidirectional UHTCMCs for extreme environments, Sci. Rep. 8 (2018) 9148, https://doi.org/10.1038/s41598-018-27328-x.